A Generalized and Efficient Control-Oriented Modeling Approach for Vibration-Prone Delta 3D Printers Using Receptance Coupling

Nosakhare Edoimioya and Chinedum E. Okwudire, *Member, IEEE*

***Abstract*— Delta 3D printers can significantly increase throughput in additive manufacturing by enabling faster and more precise motion compared to conventional serial-axis 3D printers. Further improvements in motion speed and part quality can be realized through model-based feedforward vibration control, as demonstrated on serial-axis 3D printers. However, delta machines have not benefited from model-based controllers because of the difficulty in accurately modeling their position-dependent, coupled nonlinear dynamics. In this paper, we propose an efficient framework to obtain accurate linear parameter-varying models of delta 3D printers at any position within their workspace from a few frequency response measurements. We decompose the dynamics into two sub-models–(1) an experimentally-identified sub-model containing decoupled vibration dynamics; and (2) an analytically-derived sub-model containing coupled dynamics–which are combined into one using receptance coupling. We generalize the framework by extending the analytical model of (2) to account for differing mass profiles and dynamic models of the printer's end-effector. Experiments demonstrate reasonably accurate predictions of the position-dependent dynamics of a commercial delta printer, augmented with a direct drive extruder, at various positions in its workspace.**

***Note to Practitioners*—This work aims to equip high-speed 3D printers, like delta machines, with model-based controllers to complement their speed with high-accuracy. Due to the coupled kinematic chains of the delta, complex control methodologies, some of which require real-time state measurements, are often used to achieve satisfactory control performance. Our modeling approach provides an efficient methodology for obtaining accurate linear models without the need for real-time measurements, thus enabling practitioners to design linear model-based feedforward controllers to achieve the high throughput and accuracy desired in additive manufacturing (AM). The models we develop in this paper are intended for use with feedforward vibration compensation methods, which can be beneficial for both industrial-scale AM machines that have high-powered servo motors and feedback controllers, as well as consumer-grade AM machines which use stepper motors in feedforward control.**

***Index Terms*— Receptance coupling, FDM 3D printing, delta robot, linear parameter-varying, position-dependent dynamics.**

I. INTRODUCTION

THE delta robot [1], [2] is a parallel-axis manipulator that has been used in a variety of research and industrial applications [3]. Three-dimensional printers with a delta kinematic configuration are primarily used with fused filament fabrication (FFF) additive manufacturing (AM) technology. These printers use three actuators to move three prismatic joints, which are all connected to the end-effector in parallel via forearm links (see Fig. 1). Vertical motion of the joints results in lateral and vertical motion of the nozzle as it extrudes and deposits material on a heated, stationary bed. As a result of the parallel-axis construction, the delta 3D printer boasts higher speeds and accelerations than conventional 3D printers with serial kinematics [4]. Furthermore, delta 3D printers can command identical speeds in all three Cartesian axes, whereas the axis speed of serial 3D printers vary–with the vertical (z) axis typically having much lower speeds than the lateral (x, y) axes [5]. Accordingly, delta printers have expanded the capabilities of FFF and, for example, have been shown to improve the quality of Curved Layer FFF [6], which varies the z-axis position within layers. Examples of commercial delta 3D printers (at the time of this writing) include the Monoprice (MP) Delta Pro [7], the FLSUN QQ-S Pro [8], the Delta WASP 2040 [9], and the Tractus T3500 [10].

Much like serial machines, delta 3D printers experience undesirable vibration when they travel at high speeds due to structural flexibilities in their kinematic chain [5]. Feedforward (FF) model-based control techniques have been used to compensate vibration in serial 3D printers resulting in an order of magnitude increase in achievable accelerations and up to 2x reduction in print time without sacrificing quality [11]–[14]. Accurate models of most serial 3D printers are efficiently measured by treating them as linear time-invariant (LTI) single-input, single-output (SISO) systems [11]–[14]. In contrast, parallel-axis 3D printers are more likely to be position-dependent multiple-input, multiple-output systems [15], [16]. Thus, identifying their dynamics can be time-consuming because one must measure the models at several different positions. Analytical models can be derived but they may be: (a) too complex to be suitable for real-time

---

Manuscript received 8 June 2022; accepted 1 August 2022. This article was recommended for publication by Editor X. Xie upon evaluation of the reviewers' comments. This work was supported in part by the National Science Foundation under Grant 2054715 and Grant DGE 1256260 and in part by the Michigan Space Grant Consortium, which is awarded by the National Aeronautics and Space Administration under Award 80NSSC20M0124. *(Corresponding author: Chinedum E. Okwudire.)*

The authors are with the Department of Mechanical Engineering, University of Michigan, Ann Arbor, MI 48104 USA (e-mail: okwudire@umich.edu).

Color versions of one or more figures in this article are available at https://doi.org/10.1109/TASE.2022.3197057.

Digital Object Identifier 10.1109/TASE.2022.3197057

control [17]–[19] or (b) contain a large number of parameters that are difficult to measure and identify accurately [16].

Simplifications of analytical models of delta manipulators have been proposed and used in model-based controllers [16], [20]–[24]. However, most of the previous work considers delta robots with rotary joints (instead of the prismatic joints used in delta 3D printers), which typically use servo motors with encoders. As a result, these control schemes are usually aided by feedback regulators to compensate measured (and estimated) errors [16], [21]–[29]. For example, recent work has focused on improving measurement accuracy of real-time servo errors using various techniques such as sophisticated observers [23], [24] and artificial neural networks (ANNs) [25]. The position-dependent dynamic variations of delta robots are treated as unmodeled disturbances which are suppressed using feedback control [26]–[29]. However, most commercial delta 3D printers cannot benefit from such approaches because they utilize stepper motors for actuation, which have no feedback sensors. Therefore, they must rely on models that accurately capture their dynamics without the need for real-time measurement of state variables.

Another control approach is to tune trajectory-dependent PID controller gains offline to minimize errors along a desired path of the robot [21], [22]. The PID gains are optimized for the path such that they provide reasonably good tracking performance without the need to have a general controller for the entire workspace. However, this method requires knowing the trajectory information a priori, which is not always possible.

Sparse offline measurements have also been combined with other techniques, like interpolation [30] and machine learning [31], to predict position-dependent dynamics of manufacturing machines. Voorhoeve *et al.* [30] measured LTI models of a flexible wafer stage at several frozen positions and then interpolated the mode shapes to obtain a model with continuous position dependence. However, their approach requires a large number of measurements which could be prohibitive. Additionally, the approach was implemented on a single flexible moving body and it is not clear how it translates to systems with multiple (and coupled) moving bodies like the delta manipulator. To eliminate the need for time-consuming measurements, Liu and Altintas [31] trained a transfer learning model using two ANNs: the first using abundant data from the simulated dynamics of a machine, and the second with significantly less measurements from the machine. The models were combined to fine-tune the simulation model with the "real-world" model. Despite the success of this technique, it requires the laborious process of tuning hyperparameters during training. Additionally, since these models often lack physical interpretation, designing stable controllers for them can be challenging. Fortunately, receptance coupling (RC) [32] provides an avenue to efficiently and accurately model manufacturing machines offline while retaining physical understanding. It allows one to combine analytical models and sparse measurements of sub-assemblies of a system to form the full assembly's frequency response function (FRF) [33], [34]. RC simplifies modeling by providing flexibility in circumstances where it is difficult or impossible to obtain either: (a) measurements that describe the full assembly or (b) an analytical model that is computationally efficient for real-time control and whose parameters can be easily identified.

In a preliminary version of this paper [35], we introduced the idea of modeling delta 3D printers using RC. However, the approach was narrow because it assumed the end-effector distributes mass equally (i.e., symmetrically) to each carriage and could be modeled as a rigid body. While these assumptions may be reasonable for a specific delta printer, they do not generally hold true. For example, delta printers may use a direct drive filament extruder rather than the Bowden-style extruder used in [35]. Depending on the size, shape, design, and fabrication of the extruder, the end-effector may have an asymmetric mass distribution and flexible dynamics. To account for such circumstances, this paper builds on the preliminary work to make the following contributions:

1) It generalizes the RC framework for modeling the position-dependent and coupled dynamics of delta 3D printers to include different mass distributions and dynamic models of the end-effector;
2) It proposes an efficient methodology for identifying the generalized model with only a few measurements at one location; and
3) It demonstrates, through experiments on a commercial delta 3D printer, that the generalized model yields reasonably accurate predictions of the dynamics of the machine in arbitrary configurations.

The rest of the paper is as follows: Section II briefly describes the construction of the delta 3D printer; Section III describes the RC framework and generalized model; Section IV uses data from a commercial 3D printer to identify the parameters of the model and validates it by comparing the predicted model with measured data; and Sections V and VI present a discussion and our conclusions, respectively.

II. DESCRIPTION OF THE DELTA 3D PRINTER

The three pairs of forearms on the delta 3D printer are connected to a carriage on one end and an end-effector on the other end; the forearms are allowed to rotate freely about universal joints. In the case of the MP Delta Pro 3D printer shown in Fig. 1 (as well as several commercial printers), the universal joints are iron balls which allow the magnetized ends of the forearms to be detached and reattached by the user. On the carriage end, each carriage is mounted to a timing belt, which is, in turn, connected to a base-mounted stepper motor via a pulley. The vertical positions of each carriage (the joint space) determine the Cartesian position of the 3-DOF end-effector (the task space). The parallelogram formed by each pair of forearms guarantees that the end-effector and bed remain co-planar for layer-by-layer printing.

The kinematics of the delta manipulator are characterized by a set of nonlinear, holonomic spherical constraint equations that relate the task and joint spaces, such that the motion of one carriage may have an effect on other carriages and vice versa. As a result, the dynamics of the printer vary from position to position [16], [35].

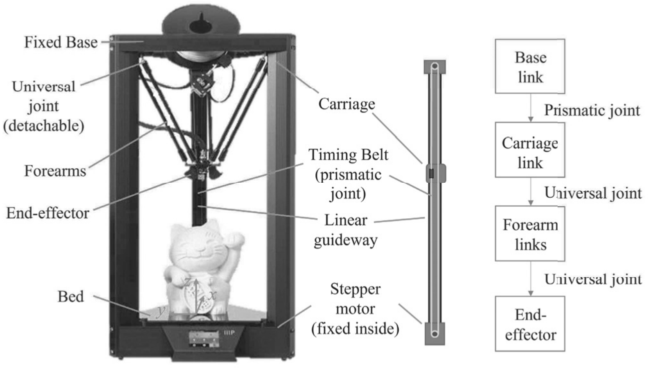

Fig. 1. From left to right: A commercial delta 3D printer (Monoprice Delta Pro) with labeled components, a schematic of the belt-driven carriage system, and the delta manipulator configuration showing the connections between joints and links. The print volume dimensions are 270 × 270 × 300 mm.

III. GENERALIZED DELTA MODEL

To derive the model of the delta printer using RC, we begin by decomposing the model of the full assembly into two sub-models. Sub-model 1 describes the carriage output position q_i as a function of two inputs: (a) the desired position of the carriage q_{d_i} and (b) the forces F_{q_i} imposed on the carriage due to the dynamics of the forearms and end-effector, where $i \in \{A, B, C\}$ denotes the carriages labeled A, B, and C (see Fig. 2). Sub-model 2 models the relationship between the end-effector's position $\mathbf{X} = [x \quad y \quad z]^T$ and F_{q_i}.

Sub-model 1 decouples each carriage as though they are disconnected from the end-effector. Accordingly, the model is assumed to be linear since each carriage consists of the carriage mass and timing belt, which can be modeled as a mass-spring-damper system [11]–[14]. The relationship between the inputs and q_i are given by continuous-time LTI SISO systems $G_{q_{d_i}}(s)$, the carriage position to position FRF, and $G_{Fq_i}(s)$, the external force to carriage position FRF. Both SISO systems are measured (or modeled analytically) from experiments as a summation of vibration modes, such that

$$q_i(s) = G_{q_{d_i}}(s) q_{d_i}(s) + G_{Fq_i}(s) F_{q_i}(\mathbf{X}, s) \tag{1}$$

where s is the Laplace variable and F_{q_i} is a function of $\mathbf{X}$. Since each carriage is identical, we assume the SISO FRFs are identical for each carriage, i.e., $G_{q_{d_i}}(s) = G_{q_d}(s)$ and $G_{Fq_i}(s) = G_{Fq}(s)$ for all i.

Sub-model 2 connects the end-effector to the carriages through F_{q_i} in Eq. 1. Therefore, it incorporates the flexible dynamics of the forearms and the end-effector (henceforth simply referred to as the end-effector dynamics). The expression of $F_{q_i}(\mathbf{X}, s)$ is characterized by the Jacobian matrix, which relates the joint space and task space velocities [16] as

$$\dot{\mathbf{X}} = \mathbf{J}\dot{\mathbf{q}} \tag{2}$$

where $\mathbf{q} = [q_A \quad q_B \quad q_C]^T$ is the joint space coordinate vector (i.e., carriage coordinates) and $\mathbf{J} \in \mathbb{R}^{3\times 3}$ is the Jacobian matrix. Accordingly, we begin by deriving the Jacobian matrix in sub-section III-A. Then, in sub-section III-B, we use the Jacobian to derive the analytical relationship between $\mathbf{X}$ and F_{q_i}.

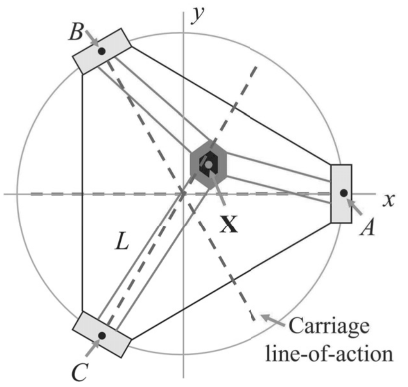

Fig. 2. Overhead view of the delta 3D printer showing the (x, y)-coordinate locations of carriages A, B, and C, the end-effector's position in task space $\mathbf{X}$, and the length of the forearms L. End-effector motion along a carriage's line-of-action, referred to in Section IV, results in significant change to the carriage dynamics.

A. Sub-Model 2: The Jacobian Matrix

The Jacobian is derived based on work from [16]. Without loss of generality, we locate the origin of the task space coordinate system at the center of the bed and align the x-axis with the center of carriage A. Carriages B and C are spaced 120° apart from A and from each other (Fig. 2). All forearms are identical and have length L and position $\mathbf{X}$ is at the center of the end-effector platform–on the xy-plane intersecting the forearm/end-effector connection points. The vertical distance from this plane down to the tip of the hot-end is given by H_{ez} (see Fig. 3(a)). The spherical constraint equations that govern the kinematics are given by

$$(x - A_x)^2 + (y - A_y)^2 + (z + H_{ez} - q_A)^2 = L^2 \tag{3}$$

$$(x - B_x)^2 + (y - B_y)^2 + (z + H_{ez} - q_B)^2 = L^2 \tag{4}$$

$$(x - C_x)^2 + (y - C_y)^2 + (z + H_{ez} - q_C)^2 = L^2 \tag{5}$$

where (A_x, A_y) are the x- and y-axis coordinates of carriage A and similarly for carriages B and C. We can write Eqs. 3-5 in vector form as

$$\mathbf{s}_i^T \mathbf{s}_i - L^2 = 0 \tag{6}$$

where

$$\mathbf{s}_i = \begin{bmatrix} x - i_x \\ y - i_y \\ z + H_{ez} - q_i \end{bmatrix} = \begin{bmatrix} x \\ y \\ z \end{bmatrix} - \left(\begin{bmatrix} i_x \\ i_y \\ -H_{ez} \end{bmatrix} + \begin{bmatrix} 0 \\ 0 \\ 1 \end{bmatrix} q_i \right) \tag{7}$$

Taking the time derivative of Eq. 6 yields

$$\mathbf{s}_i^T \dot{\mathbf{s}}_i + \dot{\mathbf{s}}_i^T \mathbf{s}_i = 0 \tag{8}$$

which, from the commutative property of the vector product, can be rewritten as

$$\mathbf{s}_i^T \dot{\mathbf{s}}_i = 0 \tag{9}$$

where

$$\dot{\mathbf{s}}_i = \begin{bmatrix} \dot{x} \\ \dot{y} \\ \dot{z} \end{bmatrix} + \begin{bmatrix} 0 \\ 0 \\ -1 \end{bmatrix} \dot{q}_i = \dot{\mathbf{X}} + \mathbf{p}\dot{q}_i. \tag{10}$$

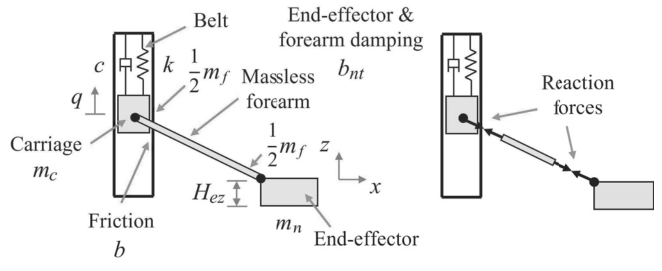

(a) (b)

Fig. 3. (a) Modeling schematic for delta 3D printer showing the belt-carriage system modeled as a mass-spring-damper system and, as done in Section IV, the forearm modeled as a massless entity with its mass split between the carriage and end-effector; (b) the forearm transmits reaction forces between the end-effector and the carriage.

Rearranging Eq. 9 with the definition of $\mathbf{p}$, we have

$$\begin{bmatrix}\mathbf{s}_A^T\\ \mathbf{s}_B^T\\ \mathbf{s}_C^T\end{bmatrix}\dot{\mathbf{X}}+\begin{bmatrix}\mathbf{s}_A^T\mathbf{p}&0&0\\0&\mathbf{s}_B^T\mathbf{p}&0\\0&0&\mathbf{s}_C^T\mathbf{p}\end{bmatrix}\dot{\mathbf{q}}=\begin{bmatrix}0\\0\\0\end{bmatrix}. \tag{11}$$

From Eq. 11, we can obtain the relation in Eq. 2 where

$$\mathbf{J}=-\begin{bmatrix}\mathbf{s}_A^T\\ \mathbf{s}_B^T\\ \mathbf{s}_C^T\end{bmatrix}^{-1}\begin{bmatrix}\mathbf{s}_A^T\mathbf{p}&0&0\\0&\mathbf{s}_B^T\mathbf{p}&0\\0&0&\mathbf{s}_C^T\mathbf{p}\end{bmatrix}. \tag{12}$$

After another time derivative of Eq. 11 and some transformations, we find the task space acceleration $\ddot{\mathbf{X}}$ as

$$\ddot{\mathbf{X}}=\begin{bmatrix}\mathbf{s}_A^T\\ \mathbf{s}_B^T\\ \mathbf{s}_C^T\end{bmatrix}^{-1}\left(\begin{bmatrix}\dot{\mathbf{s}}_A^T\\ \dot{\mathbf{s}}_B^T\\ \dot{\mathbf{s}}_C^T\end{bmatrix}\mathbf{J}+\mathbf{T}\right)\dot{\mathbf{q}}+\mathbf{J}\ddot{\mathbf{q}}=\mathbf{J}\ddot{\mathbf{q}}+\dot{\mathbf{J}}\dot{\mathbf{q}} \tag{13}$$

where

$$\mathbf{T}=\begin{bmatrix}\dot{\mathbf{s}}_A^T\mathbf{p}&0&0\\0&\dot{\mathbf{s}}_B^T\mathbf{p}&0\\0&0&\dot{\mathbf{s}}_C^T\mathbf{p}\end{bmatrix}.$$

B. Sub-Model 2: End-Effector Position to Carriage Forces

To find the exogenous force F_{q_i} imposed on each carriage, we first write the force and moment (torque) balance equations about the end-effector's center of mass in task space coordinates. Then, we transform the resulting reaction forces to joint space coordinates using the Jacobian matrix. From the free body diagram in Fig. 4, the forces on the end-effector (in the Laplace domain) are given by

$$F_{Ax}(s)+F_{Bx}(s)+F_{Cx}(s)=w_x(s)x(s) \tag{14}$$

$$F_{Ay}(s)+F_{By}(s)+F_{Cy}(s)=w_y(s)y(s) \tag{15}$$

$$F_{Az}(s)+F_{Bz}(s)+F_{Cz}(s)=w_z(s)z(s) \tag{16}$$

where $\mathbf{F}_A=[F_{Ax}\quad F_{Ay}\quad F_{Az}]^T$ are the respective x-, y-, and z-axis components of the force on the end-effector associated with carriage A, similarly for $\mathbf{F}_B=[F_{Bx}\quad F_{By}\quad F_{Cz}]^T$ and $\mathbf{F}_C=[F_{Cx}\quad F_{Cy}\quad F_{Cz}]^T$, and w_x, w_y, and w_z are the flexible inertial dynamics of the end-effector in the x-, y-, and z-axis directions. (Note that we will, henceforth, omit the Laplace variable s in the paragraph text for simplicity when it is understood in context.)

Remark III(a): Here, we assume that the inertial dynamics are decoupled in the task space coordinates since the machine is designed to produce independent motion in each direction. However, the approach can be easily generalized for coupled dynamics in the task space coordinates.

We can compactly express the force equations as

$$\mathbf{F}_A(s)+\mathbf{F}_B(s)+\mathbf{F}_C(s)=\mathbf{W}(s)\mathbf{X}(s) \tag{17}$$

where

$$\mathbf{W}(s)=\begin{bmatrix}w_x(s)&0&0\\0&w_y(s)&0\\0&0&w_z(s)\end{bmatrix}. \tag{18}$$

Since the end-effector does not rotate during motion, the moment equations about the center of mass are given by

$$\mathbf{r}_A\times\mathbf{F}_A(s)+\mathbf{r}_B\times\mathbf{F}_B(s)+\mathbf{r}_C\times\mathbf{F}_C(s)=\mathbf{0}_{3\times 1} \tag{19}$$

where

$$\mathbf{r}_i=\begin{bmatrix}D_e\cos(\phi_i)-\delta_x\\ D_e\sin(\phi_i)-\delta_y\\ -\delta_z\end{bmatrix}, \tag{20}$$

δ_x, δ_y, and δ_z are the x- y- and z-coordinate distance from the centroid to the center of mass, D_e is the distance from the centroid to the forearm reaction force, and ϕ_i is the angle where carriage i is located with respect to the global x-axis on the horizontal plane (see Fig. 4). For simplicity, we neglect rotational effects of forearms, which have been found to be negligible [16], [36].

We can compute the reaction forces $\mathbf{F}_A$, $\mathbf{F}_B$, $\mathbf{F}_C$ as a function of the end-effector's motion by writing the six equations of motion in matrix form as

$$\underbrace{\begin{bmatrix}\mathbf{I}&\mathbf{I}&\mathbf{I}\\ \mathbf{S}(\mathbf{r}_A)&\mathbf{S}(\mathbf{r}_B)&\mathbf{S}(\mathbf{r}_C)\end{bmatrix}}_{\mathbf{L}}\underbrace{\begin{bmatrix}\mathbf{F}_A(s)\\ \mathbf{F}_B(s)\\ \mathbf{F}_C(s)\end{bmatrix}}_{\mathbf{f}(s)}=\underbrace{\begin{bmatrix}\mathbf{W}(s)\mathbf{X}(s)\\ \mathbf{0}_{3\times 1}\end{bmatrix}}_{\mathbf{u}(s)}, \tag{21}$$

where $\mathbf{I}\in\mathbb{R}^{3\times 3}$ is the identity matrix and $\mathbf{S}(\cdot)\in\mathbb{R}^{3\times 3}$ is the skew symmetric matrix defined on the input vector. The minimum norm solution for $\mathbf{f}$ is given by

$$\mathbf{f}(s)=\mathbf{L}^T(\mathbf{L}\mathbf{L}^T)^{-1}\mathbf{u}(s)=\mathbf{L}^{\dagger}\mathbf{u}(s) \tag{22}$$

where $\mathbf{L}^{\dagger}$ is the Moore-Penrose pseudoinverse of $\mathbf{L}$. Note that since the bottom-half rows of $\mathbf{u}$ contain zeros, the last 3 columns of $\mathbf{L}^{\dagger}\in\mathbb{R}^{9\times 6}$ do not contribute to the reaction forces. Thus, we can use a reduced matrix $\tilde{\mathbf{L}}^{\dagger}\in\mathbb{R}^{9\times 3}$ and the reaction forces (i.e., each row of $\mathbf{f}$) can be written independently as

$$\mathbf{F}_i(s)=\mathbf{P}_i\mathbf{W}(s)\mathbf{X}(s) \tag{23}$$

where $\mathbf{P}_i\in\mathbb{R}^{3\times 3}$ is the matrix of constants representing the distribution of task space forces associated with carriage i, which is extracted from respective portions of $\tilde{\mathbf{L}}^{\dagger}$. Each force can be transformed to the joint space using $\bar{\mathbf{J}}_i\in\mathbb{R}^{3\times 1}$, the column vector extracted from the linearized Jacobian, denoted by $\bar{\mathbf{J}}$. The transpose of $\bar{\mathbf{J}}_i$ transforms the task space coordinates

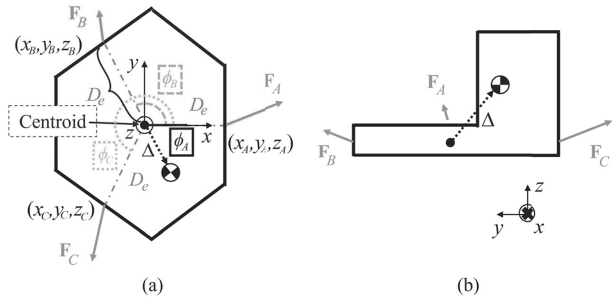

(a)

(b)

Fig. 4. (a) Top view and (b) side view free body diagrams of the end-effector with reaction force vectors from each forearm. Note that the center of mass is not located at the centroid of the end-effector, which leads to an uneven distribution of reaction forces. The vector difference between the centroid and the center of mass is given by $\Delta = [\delta_x \quad \delta_y \quad \delta_z]^T$.

of the reaction joint associated with carriage i, denoted by (x_i, y_i, z_i), to the joint space coordinate q_i (see Fig. 4(a)).

Remark III(b) [35]: The linearized Jacobian is obtained by linearizing Eqs. 2 and 13 about an equilibrium position denoted by

$$\bar{\mathbf{X}} = \begin{bmatrix} \bar{x} \\ \bar{y} \\ \bar{z} \end{bmatrix} \text{ and } \bar{\mathbf{q}} = \begin{bmatrix} \bar{q}_A \\ \bar{q}_B \\ \bar{q}_C \end{bmatrix}. \tag{24}$$

The transformed (and linearized) force is given by

$$F_{q_i} = \bar{\mathbf{J}}_i^T \mathbf{F}_i(s) = \bar{\mathbf{J}}_i^T \mathbf{P}_i \mathbf{W}(s) \mathbf{X}(s). \tag{25}$$

Furthermore, we can substitute the Jacobian relationship from Eq. 2 such that Eq. 25 becomes

$$F_{q_i} = \bar{\mathbf{J}}_i^T \mathbf{P}_i \mathbf{W}(s) \bar{\mathbf{J}} \mathbf{q}(s) \tag{26}$$

Finally, we can write the full model in the form of Eq. 1:

$$\mathbf{q}(s) = \mathbf{G}_{q_d}(s)\mathbf{q}_d(s) + \mathbf{G}_{Fq}(s) \begin{bmatrix} \bar{\mathbf{J}}_A^T \mathbf{P}_A \\ \bar{\mathbf{J}}_B^T \mathbf{P}_B \\ \bar{\mathbf{J}}_C^T \mathbf{P}_C \end{bmatrix} \mathbf{W}(s) \bar{\mathbf{J}} \mathbf{q}(s) \tag{27}$$

where $\mathbf{G}_{q_d}(s)$ and $\mathbf{G}_{Fq}(s)$ are 3×3 diagonal matrices that contain $G_{q_d}(s)$ and $G_{Fq}(s)$, respectively, as the diagonal entries. The model can be expressed simply as

$$\mathbf{q}(s) = \mathbf{G}(s)\mathbf{q}_d(s) \tag{28}$$

where

$$\mathbf{G}(s) = \left[\mathbf{I} - \mathbf{G}_{Fq}(s) \begin{bmatrix} \bar{\mathbf{J}}_A^T \mathbf{P}_A \\ \bar{\mathbf{J}}_B^T \mathbf{P}_B \\ \bar{\mathbf{J}}_C^T \mathbf{P}_C \end{bmatrix} \mathbf{W}(s) \bar{\mathbf{J}} \right]^{-1} \mathbf{G}_{q_d}(s), \tag{29}$$

yielding a linear parameter-varying (LPV) model of the delta 3D printer that can be used for model-based control. In Section IV, we present an example where $\mathbf{G}_{q_d}(s)$, $\mathbf{G}_{Fq}(s)$, $\mathbf{W}(s)$, and other parameters are identified for a delta printer with a flexible, two-mass end-effector. The parameters of the model are efficiently identified using data measured at one position, and used to predict FRFs at other positions.

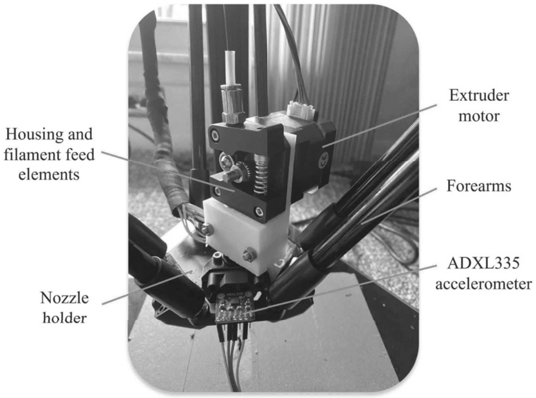

Fig. 5. Image of a prototype of the direct drive extruder mounted on the MP Delta Pro 3D printer with the nozzle holder, extruder motor and housing labeled. The assembly is designed to fit within the existing end-effector platform without obstructing the forearm motion during printing. The ADXL335 accelerometers (pictured) were used to measure frequency response functions.

IV. EXPERIMENTAL VALIDATION

To study the framework described above, we identify the model of the MP Delta Pro 3D printer in this section. The printer is sold with a Bowden-style extruder [15] but we augmented it with a direct-drive extruder (shown in Fig. 5) to enhance extrusion performance [37]. Source files of the extruder design can be found on Thingiverse.[1]

A. Decoupled Carriage Model Identification (Sub-Model 1)

The modular nature of commercial delta 3D printers is an advantage in determining the FRFs because we can detach the forearms and the end-effector to measure the carriage position to position FRF, G_{q_d}. As in [16], the mass of the forearms is assumed to be split equally between the carriage and the end-effector (see Fig. 3(a)). Then, G_{q_d} can be represented (mechanically) as a mass-spring-damper system with stiffness k, belt damping coefficient c, guideway friction b, and mass

$$m = m_c + \frac{1}{2} m_f \tag{30}$$

where m_c is the lumped mass of the carriage assembly and m_f is the mass of a pair of forearms (Fig. 3).

The carriage FRF is identified from acceleration data measured using ADXL335 accelerometers on the carriage, with the end-effector detached but one of two forearms still attached (as in Eq. 30). We used a dSPACE MicroLabBox and Pololu stepper motor drivers (DRV8825) to command sine sweep perturbations around carriage positions corresponding to the task space positions $(x, y, z) = (0, 0, 30)$, $(0, 0, 50)$, $(0, 0, 70)$ mm. As expected, our measurements indicated that G_{q_d} was similar at the three locations, independent of the z-axis position, so we used the data from $(0, 0, 30)$ mm, shown in Fig. 6, to fit a 4th-order FRF of the form

$$G_{q_d}(s) = G_{q_{d,m}}(s) G_{q_{d,e}}(s), \tag{31}$$

---

[1] Extruder design source files can be found at the following Thingiverse directory: https://www.thingiverse.com/ahasib/collections/direct-drive-extruder-mount-for-delta-printer

where $G_{q_{d,m}}(s)$ and $G_{q_{d,e}}(s)$ represent the mechanical and electrical dynamics, respectively. (The electrical dynamics are created by the electrical circuitry that generates the stepper motor commands.) Hence, we have

$$G_{q_{d,m}}(s) = \frac{cs+k}{ms^2+(c+b)s+k} \tag{32}$$

$$= \frac{\frac{c}{m}s+\omega_n^2}{s^2+2\zeta\omega_n s+\omega_n^2} \tag{33}$$

and

$$G_{q_{d,e}}(s) = \frac{d_1 s+d_0}{s^2+d_2 s+d_0} \tag{34}$$

where ω_n is the natural frequency, ζ is the damping ratio,

$$2\zeta\omega_n = (c+b)/m, \tag{35}$$

$$\omega_n^2 = k/m, \tag{36}$$

and d_0, d_1, and d_2 are the coefficients of the electrical FRF. To determine the m, and therefore m_c (since m_f can be measured directly), we conducted the same sine sweep experiment with an additional mass $m_{add} = 200$ g mounted to the carriage. This experiment also generates mechanical FRFs that are identical for each carriage, one of which is shown in Fig. 7 and given by

$$G'_{q_{d,m}}(s) = \frac{cs+k}{m's^2+(c+b)s+k} \tag{37}$$

$$= \frac{\frac{c}{m'}s+\omega_n'^2}{s^2+2\zeta'\omega_n' s+\omega_n'^2} \tag{38}$$

where $m' = m + m_{add}$,

$$2\zeta'\omega_n' = (c+b)/m', \tag{39}$$

and

$$\omega_n'^2 = k/m'. \tag{40}$$

From Eqs. 36 and 40, m can be computed as

$$m = \frac{\omega_n'^2}{(\omega_n^2 - \omega_n'^2)} m_{add} \tag{41}$$

and Eqs. 35 and 39 can be used to determine c and b. Similarly, Eq. 36 can be used to determine k. Additionally, the fitted 4th-order FRF of Eq. 31 can also be represented as

$$G_{q_d}(s) = \frac{g_2 s^2+g_1 s+g_0}{s^4+h_3 s^3+h_2 s^2+h_1 s+h_0} \tag{42}$$

where $g_{(\cdot)}$ and $h_{(\cdot)}$ are the coefficients of the fit. From the coefficients of Eqs. 31 and 42, we can write the set of equations

$$\begin{aligned} g_2 &= \frac{c}{m}d_1, \quad g_1 = \frac{c}{m}d_0 + \omega_n^2 d_1, \quad g_0 = \omega_n^2 d_0, \\ h_3 &= d_2 + 2\zeta\omega_n, \quad h_2 = d_0 + \omega_n^2 + 2\zeta\omega_n d_2, \\ h_1 &= \omega_n^2 d_2 + 2\zeta\omega_n d_0, \text{ and } h_0 = \omega_n^2 d_0. \end{aligned} \tag{43}$$

Using the fitted coefficients and computed parameters above, we can solve a least-squares problem to find d_0, d_1, and d_2.

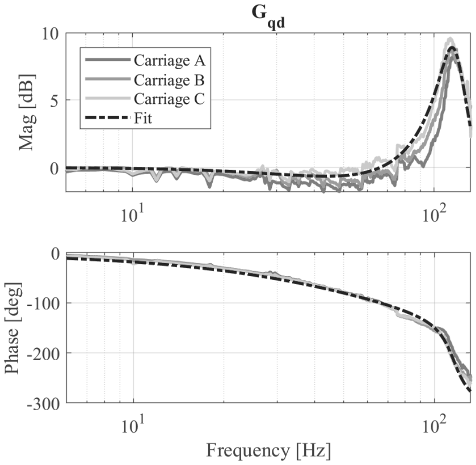

Fig. 6. Position-to-position frequency response functions of the carriage *without* the end-effector dynamics, G_{q_d}. The data was measured for each carriage at the carriage locations (q_A, q_B, q_C) corresponding to $(x, y, z) = (0, 0, 30)$ mm, and a linear fit of one of the of the frequency response functions shown as the black dashed line.

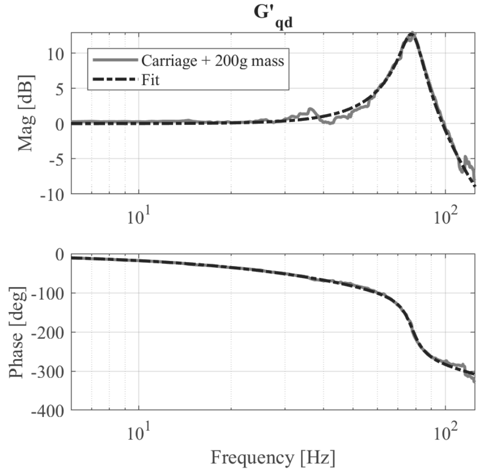

Fig. 7. Position-to-position frequency response function of the carriage *without* the end-effector dynamics but with an additional 200 g mass attached to the carriage, G'_{q_d}. The linear fit (shown as the black dashed line) is used to identify the mass of the carriage m. Note that only one carriage FRF is shown since the carriage FRFs are similar as shown in Fig. 6.

Finally, the force to position FRF is given by the (mechanical) characteristic polynomial

$$G_{Fq}(s) = -\frac{1}{ms^2+(c+b)s+k} \tag{44}$$

where the negative sign indicates that the forces involved are disturbance forces. The parameters for G_{q_d} and, therefore, G_{Fq} are reported in Table I.

B. End-Effector Model Identification (Sub-Model 2)

To identify the inertial forces from the end-effector motion (Eq. 25), we assume the end-effector can be modeled as a two-mass system–the nozzle holder mass and the extruder motor mass–with a spring and damper between the masses. We validate this assumption by isolating the end-effector and

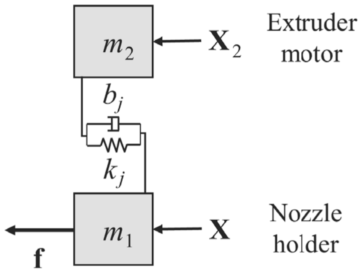

Fig. 8. Schematic of the two-mass model of the direct drive extruder (end-effector) with the flexible components between the extruder motor and the nozzle holder modeled as a spring-damper system. The damping and spring coefficient, b_j and k_j, respectively, are defined on each axis of the task space (i.e., $j \in \{x, y, z\}$). The relative positions of the nozzle holder and the extruder motor are indicated by $\mathbf{X} = [x \quad y \quad z]^T$ and $\mathbf{X}_2 = [x_2 \quad y_2 \quad z_2]^T$, respectively. The reaction forces on the nozzle holder are indicated by $\mathbf{f}$.

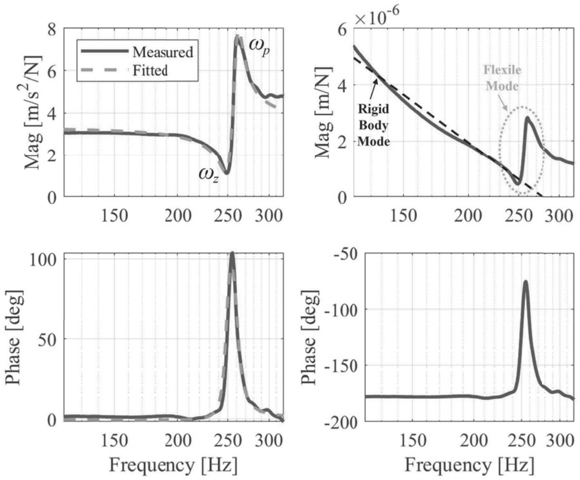

Fig. 9. Open loop force to acceleration (left) and force to position (right) FRFs of the end-effector from impact hammer experiments. The force to position FRF is estimated at the discrete integral of the measured force to acceleration FRF to show the rigid body and flexible modes indicating a two-mass model of the end-effector. The labels ω_z and ω_p indicate the zero and pole location of the two-mass model, respectively.

measuring the open loop force to acceleration FRF of the nozzle holder mass, m_1, using a PCB Piezotronics® impact hammer (model #086C03); the impact hammer was used to apply a force to m_1–similar to what is shown in Fig. 8. Figure 9 shows the measured force to acceleration FRF as well as the computed force to position FRF, which has the characteristic rigid body and flexible modes of a two-mass model. We can derive the force to acceleration FRF of m_1 model and fit the measurement in Fig. 9 with a second-order model to identify the masses. The two FRFs are represented by

$$\frac{s^2 X_{act}(s)}{F_h(s)} = \frac{m_2 s^2 + b_{act} s + k_{act}}{m_1 m_2 s^2 + (m_1 + m_2) b_{act} s + (m_1 + m_2) k_{act}} \tag{45}$$

$$= \frac{u_2 s^2 + u_1 s + u_0}{s^2 + v_1 s + v_0} \tag{46}$$

where m_2 is the extruder motor mass, b_{act} and k_{act} are the damping and stiffness constants in the direction activated by the impact hammer, $u_{(\cdot)}$ and $v_{(\cdot)}$ are the coefficients of the fitted FRF, and X_{act} and F_h are the position of m_1 and impact hammer force on m_1, respectively. Let ω_z and ω_p be the magnitude of the zero and pole location of the fitted FRF in Eq. 46, respectively. Then, it can be shown that

$$\omega_z^2 = \frac{k_{act}}{m_2} \tag{47}$$

$$\omega_p^2 = \frac{(m_1 + m_2) k_{act}}{m_1 m_2} \tag{48}$$

Solving Eqs. 47 and 48 simultaneously, we have

$$\frac{\omega_z^2}{\omega_p^2} = \frac{m_1}{m_1 + m_2} \Rightarrow m_1 = \frac{\omega_z^2}{\omega_p^2}(m_1 + m_2) \tag{49}$$

The mass of the nozzle holder, extruder motor, and housing elements can be measured with a scale to obtain the total mass, $m_{tot} = m_1 + m_2$. Therefore, m_1 and $m_2 = m_{tot} - m_1$ can be identified. Importantly, note that the values of b_{act} or k_{act} do not need to be known to identify m_1 and m_2. The measurement direction of the accelerometer simply needs to be parallel to the impact hammer force vector.

Using the two-mass model, we can write the set of force equations from Eqs. 14-16 for the nozzle holder and the extruder motor mass, which will be used to determine $\mathbf{W}(s)$ in Eq. 25. The equations for the nozzle holder are given by

$$F_{Ax} + F_{Bx} + F_{Cx} = m_1 \ddot{x} + b_x \dot{x} + k_x x - b_x \dot{x}_2 - k_x x_2 \tag{50}$$

$$F_{Ay} + F_{By} + F_{Cy} = m_1 \ddot{y} + b_y \dot{y} + k_y y - b_y \dot{y}_2 - k_y y_2 \tag{51}$$

$$F_{Az} + F_{Bz} + F_{Cz} = m_1 \ddot{z} + b_z \dot{z} + k_z z - b_z \dot{z}_2 - k_z z_2 \tag{52}$$

where the reaction forces are as described in Section III, b_x, b_y, and b_z are the damping coefficients in the x-, y- and z-axis directions, respectively, k_x, k_y, and k_z are the stiffness coefficients in the respective directions, and the subscript "2" denotes the coordinate system for the extruder motor. Note that in Eqs. 50-52, we assume that the effect of cross stiffness and damping terms (e.g., x-to-y terms b_{xy}, k_{xy}) are negligible since the motion that each axis induces on the other two axes is negligible. For the extruder motor, the force equations are given by

$$b_x \dot{x} + k_x x = m_2 \ddot{x}_2 + b_x \dot{x}_2 + k_x x_2 \tag{53}$$

$$b_x \dot{y} + k_x y = m_2 \ddot{y}_2 + b_x \dot{y}_2 + k_x y_2 \tag{54}$$

$$b_x \dot{z} + k_x z = m_2 \ddot{z}_2 + b_x \dot{z}_2 + k_x z_2. \tag{55}$$

Let $\mathbf{X}_2 = [x_2 \quad y_2 \quad z_2]^T$ be m_2's position. Then we can write Eqs. 53-55 in Laplace form as

$$\left[(\mathbf{M}_2 s^2 + \mathbf{B}s + \mathbf{K})^{-1}(\mathbf{B}s + \mathbf{K})\right]\mathbf{X}(s) = \mathbf{X}_2(s) \tag{56}$$

where

$$\mathbf{M}_2 = \begin{bmatrix} m_2 & 0 & 0 \\ 0 & m_2 & 0 \\ 0 & 0 & m_2 \end{bmatrix}, \tag{57}$$

$$\mathbf{B} = \begin{bmatrix} b_x & 0 & 0 \\ 0 & b_y & 0 \\ 0 & 0 & b_z \end{bmatrix}, \tag{58}$$

and

$$\mathbf{K} = \begin{bmatrix} k_x & 0 & 0 \\ 0 & k_y & 0 \\ 0 & 0 & k_z \end{bmatrix}. \tag{59}$$

After computing the Laplace transform of Eqs. 50-52 and substituting $\mathbf{X}_2$ into Eqs. 50-52, we obtain a vector equation of the end-effector assembly in the form of Eq. 17:

$$\mathbf{F}_A(s) + \mathbf{F}_B(s) + \mathbf{F}_C(s) = \mathbf{W}(s)\mathbf{X}(s) \tag{60}$$

where

$$\begin{aligned}\mathbf{W}(s) = {} & \mathbf{M}_1 s^2 + \mathbf{B}s + \mathbf{K} \\ & - (\mathbf{B}s + \mathbf{K})(\mathbf{M}_2 s^2 + \mathbf{B}s + \mathbf{K})^{-1}(\mathbf{B}s + \mathbf{K})\end{aligned} \tag{61}$$

and

$$\mathbf{M}_1 = \begin{bmatrix} m_1 & 0 & 0 \\ 0 & m_1 & 0 \\ 0 & 0 & m_1 \end{bmatrix}. \tag{62}$$

Note that once all parameters are identified, we can add the moment equations to write the complete set of equations, as done in Eq. 21, and follow the procedure outlined in Section III to determine the full assembly FRF (Eq. 28).

Finally, we can estimate b_j and k_j for $j \in \{x, y, z\}$ by (a) measuring the full assembly FRFs during pure x-, y-, and z-axis translational sine sweep perturbations with the end-effector attached (and positioned at $(x, y, z) = (0, 0, 30)$ mm) and (b) using the measurements in the following least squares procedure. First, let

$$\mathbf{P}_i = \begin{bmatrix} p_{i,xx} & p_{i,yx} & p_{i,zx} \\ p_{i,xy} & p_{i,yy} & p_{i,zy} \\ p_{i,xz} & p_{i,yz} & p_{i,zz} \end{bmatrix} \tag{63}$$

from Eq. 23. Then, from Eq. 18,

$$\mathbf{P}_i\mathbf{W} = \begin{bmatrix} p_{i,xx}w_x & p_{i,yx}w_y & p_{i,zx}w_z \\ p_{i,xy}w_x & p_{i,yy}w_y & p_{i,zy}w_z \\ p_{i,xz}w_x & p_{i,yz}w_y & p_{i,zz}w_z \end{bmatrix}. \tag{64}$$

Therefore, if we command only one axis (take the z-axis, for example) without moving the other two, we will get three FRF expressions representing the z-to-q_A, z-to-q_B, and z-to-q_C transfer functions. To demonstrate this effect, examine Eq. 27 when $\mathbf{X}(s)$ is substituted for $\bar{\mathbf{J}}\mathbf{q}(s)$:

$$\mathbf{q}(s) = \mathbf{G}_{q_d}(s)\mathbf{q}_d(s) + \mathbf{G}_{Fq}(s)\begin{bmatrix} \bar{\mathbf{J}}_A^T\mathbf{P}_A \\ \bar{\mathbf{J}}_B^T\mathbf{P}_B \\ \bar{\mathbf{J}}_C^T\mathbf{P}_C \end{bmatrix}\mathbf{W}(s)\mathbf{X}(s) \tag{65}$$

where the input is $\mathbf{X}(s) = [0\ 0\ z(s)]^T$. Following this procedure, we obtain nine FRFs for the task space coordinates (three FRFs for each axis) and use them to identify the end-effector's stiffness and damping parameters as follows:

First, the full assembly FRFs are fit to a 4th-order mechanical system (6th-order with electrical dynamics)

$$G''_{q_{ji,m}}(s) = \frac{b_3 s^3 + b_2 s^2 + b_1 s + b_0}{s^4 + a_3 s^3 + a_2 s^2 + a_1 s + a_0}. \tag{66}$$

As an example, the measured and fitted FRFs for the z-axis are shown in Fig. 10. It can also be shown that

$$w_j(s) = \frac{s^2(m_1 m_2 s^2 + (m_1 + m_2)b_j s + (m_1 + m_2)k_j)}{m_2 s^2 + b_j s + k_j}, \tag{67}$$

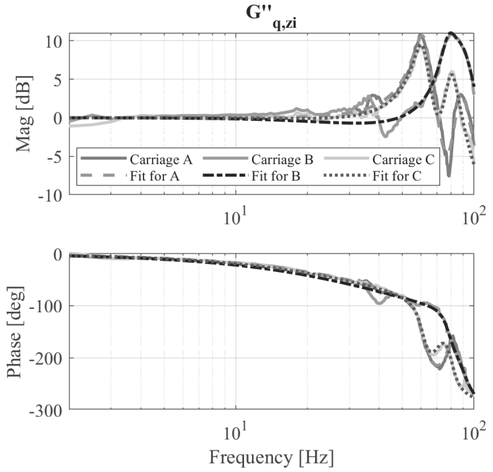

Fig. 10. Position-to-position frequency response functions of the carriage *with* the end-effector attached, $G''_{q,zi}$. The data was measured for the same carriage location as Fig. 6.

which can be substituted into Eq. 28 to obtain an expression for the characteristic polynomial of the full assembly carriage mechanical FRFs as

$$\begin{aligned} D_{ji}(s) = {} & (m + \alpha_{ji}m_1)m_2 s^4 \\ & + [(m + \alpha_{ji}(m_1 + m_2))b_j + m_2(c + b)]s^3 \\ & + [(m + \alpha_{ji}(m_1 + m_2))k_j + m_2 k + \alpha_{ji}(c + b)b_j]s^2 \\ & + ((c + b)k_j + b_j k)s + k_j k, \end{aligned} \tag{68}$$

where α_{ji} is the multiplicative factor that transforms force from the j-axis motion to the force on carriage i, and is computed as

$$\begin{bmatrix} \bar{\mathbf{J}}_A^T\mathbf{P}_A \\ \bar{\mathbf{J}}_B^T\mathbf{P}_B \\ \bar{\mathbf{J}}_C^T\mathbf{P}_C \end{bmatrix} = \begin{bmatrix} \alpha_{xA} & \alpha_{yA} & \alpha_{zA} \\ \alpha_{xB} & \alpha_{yB} & \alpha_{zB} \\ \alpha_{xC} & \alpha_{yC} & \alpha_{zC} \end{bmatrix} \tag{69}$$

with $\bar{\mathbf{J}}_i$ computed for the configuration at $(x, y, z) = (0, 0, 30)$ mm. To find $\mathbf{P}_i$, we designed a CAD model of the end-effector in SolidWorks® using the measured mass and dimensions of each component of the end-effector. From the CAD model, the center of mass of the end-effector can be automatically computed by SolidWorks® to obtain δ_x, δ_y, and δ_z and, therefore, $\mathbf{r}_i$ in Eq. 20. From Eq. 21, $\mathbf{r}_i$ is used to compute $\mathbf{L}$ and, therefore, $\tilde{\mathbf{L}}^{\dagger}$ from which $\mathbf{P}_A$, $\mathbf{P}_B$, and $\mathbf{P}_C$ are extracted. Finally, using the fitted coefficients of the characteristic polynomial in Eq. 66 (one fit for each of the nine measured FRFs), we approximate b_j and k_j in Eq. 68 via least squares using a similar process to the one outlined for Eq. 43.

Table I reports the identified parameters of the delta printer model. In the following subsection, we validate the model by comparing its predictions to measurements from the machine.

C. Validation

Since we actuate the delta printer by its carriages, predicting how the carriage dynamics vary as a function of position is paramount. By studying the dynamic variation at a few positions, we observed that the dynamics of each carriage

TABLE I

SYSTEM IDENTIFICATION PARAMETERS

Symbol	Value (units)
m_c	0.179 kg
m_f	0.032 kg
m_1	0.542 kg
m_2	0.109 kg
c	5.31 N-s/m
b	13.4 N-s/m
b_x	20.4 N-s/m
b_y	40.5 N-s/m
b_z	19.6 N-s/m
k	1.21×10^5 N/m
k_x	3.31×10^3 N/m
k_y	7.04×10^3 N/m
k_z	1.29×10^5 N/m
ω_n	730 rad/s
ω_n'	490 rad/s
ω_z	1519 rad/s
ω_p	1674 rad/s
ζ	0.092
ζ'	0.077
d_0	1.43×10^5 s^{-2}
d_1	-212.1 s^{-1}
d_2	36.2 s^{-1}
δ_x	10.21 mm
δ_y	-16.52 mm
δ_z	19.31 mm
D_e	39.91 mm

varied significantly along the carriage line-of-action: the line in the xy-plane that extends from the position of the carriage through the origin (see Fig. 2). Accordingly, we measured the full assembly carriage FRFs at $(x, y) = (-80, 0)$, $(40, -69)$ and $(40, 69)$ mm, corresponding to a distance of 80 mm from the origin along the line-of-action for carriages A, B, and C, respectively. Then, we used the identified model in Sections IV-A and IV-B to predict the same FRFs. Figures 11-13 show the predicted and measured FRF comparisons for carriages A, B, and C, respectively. In the plots, we compare the measurements to each other as well as the dynamics at $(x, y) = (0, 0)$. The major trends across the observed frequency range of the predicted and measured FRFs are similar across the sampled positions. Note that the dynamics of each carriage are different because of the asymmetric mass distribution of the end-effector. From Table I and Figure 2, note that δy is negative, meaning that the center of mass favors the side of carriages A and C causing them to hold a larger proportion of the end-effector's mass than carriage B. This phenomenon is borne out in Figs. 11-13 as carriages A and C show higher magnitude in the lower frequency mode at $(0, 0)$, while carriage B shows higher magnitude in the higher frequency mode.

Notably, the variance of the FRF at the position furthest along each carriage's line-of-action is captured by the predictions, highlighting the model's ability to capture position dependence. To quantify the similarity between the predicted and measured data, we use an error based metric. Since our FRFs are not linear with respect to frequency, common methods to quantify the goodness of fit, such as correlation coefficients, may be misleading. Table II reports the mean absolute percentage accuracy (μ_{acc}) of the predicted model, which can be thought of as how close the predicted model is to the actual measurement at each frequency. It is defined as the complement of the mean absolute percentage error (μ_{err}):

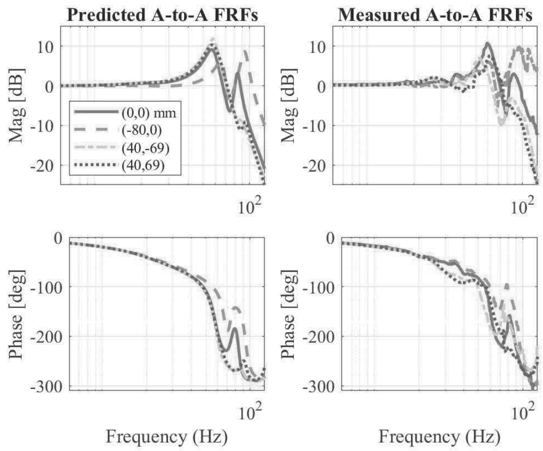

Fig. 11. Frequency response functions of the A-to-A position at $(x, y) = (0, 0)$, $(-80, 0)$, $(40, -69)$, and $(40, 69)$ ($z = 30$ mm for all) predicted with the linearized joint space FRFs from Eq. 28 (left) and measured at carriage A of the Monoprice Delta Pro 3D printer (right).

$$\mu_{acc} = 100 - \mu_{err} \tag{70}$$

$$\mu_{acc} = 100 - \left\{ \frac{1}{n} \sum_{f=f_1}^{f=f_n} \frac{|M_f - P_f|}{|M_f|} \cdot 100 \right\} \tag{71}$$

where f is the frequency, M_f are the measured data, P_f are the data from the predicted model, and $n = 247$ is the number of measured frequency points from $f_1 = 2$ Hz to $f_{247} = 125$ Hz, spaced in 0.5 Hz intervals. Note that when the prediction is perfect (i.e., $P_f = M_f$), $\mu_{err} = 0$ and $\mu_{acc} = 100\%$. As seen in Figs. 11-13 and Table II, our prediction model often has different magnitudes than the measured data at the same frequency. This indicates that there are disturbances not captured by the model. However, the average mean absolute percentage accuracy (magnitude and phase, respectively) for carriages A (67.7% and 80.0%), B (78.1% and 82.3%), and C (68.7% and 84.4%), indicate reasonable prediction accuracy of the model. Further discussion of unmodeled disturbances and potential sources of error is provided in the following section.

V. DISCUSSION

Although our magnitude predictions are inaccurate for some positions, especially positions that are not along the respective carriage's line-of-action, the frequencies at which the modes occur for each position are predicted with reasonable accuracy, which suggests that our estimates of mass and stiffness parameters are close to the true values. Sources of error in the model include: (1) the CAD model used to determine the center of mass location, which is difficult to design perfectly accurate, and (2) friction and damping, which is notoriously difficult to model. In the CAD model, we assume that each component of the end-effector has uniform distribution of mass across its volume. However, we know that some components, like the extruder motor, are composed of various metal parts with different densities that affect the distribution of mass

TABLE II

GOODNESS OF FIT BETWEEN PREDICTED AND MEASURED FRFS VIA MEAN ABSOLUTE PERCENTAGE ACCURACY (μ_{acc})

$\mu_{acc}[\%]$	$(x,y)=(0,0)$ mm		$(-80,0)$ mm		$(40,-69)$ mm		$(40,69)$ mm		Avg.	
	mag.	phase	mag.	phase	mag.	phase	mag.	phase	mag.	phase
A-to-*A*	70.1	84.7	72.6	86.0	54.6	81.6	73.6	67.7	67.7	80.0
B-to-*B*	73.1	88.8	79.4	86.6	81.1	62.2	78.7	91.5	78.1	82.3
C-to-*C*	82.5	86.5	82.1	89.8	43.7	84.7	66.5	76.7	68.7	84.4

TABLE III

PERCENT ERROR REDUCTION COMPARED TO BASELINE MODEL MEASURED AT $(0, 0)$

% error reduction	$(x,y)=(-80,0)$ mm		$(40,-69)$ mm		$(40,69)$ mm	
	mag.	phase	mag.	phase	mag.	phase
A-to-*A*	35.2	60.4	13.1	-19.8	50.6	28.6
B-to-*B*	26.9	5.8	31.9	14.2	1.1	21.3
C-to-*C*	19.4	17.6	-12.5	11.8	34.3	23.4

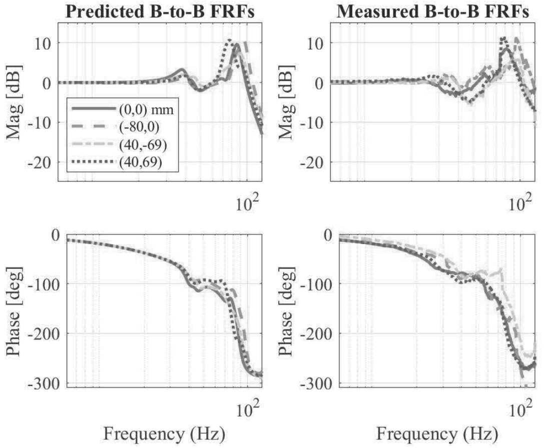

Fig. 12. Frequency response functions of the B-to-B position at $(x, y) = (0, 0)$, $(-80, 0)$, $(40, -69)$, and $(40, 69)$ ($z = 30$ mm for all) predicted with the linearized joint space FRFs from Eq. 28 (left) and measured at carriage B of the Monoprice Delta Pro 3D printer (right).

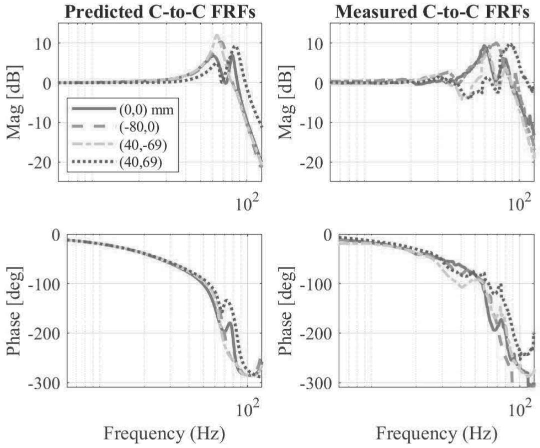

Fig. 13. Frequency response functions of the C-to-C position at $(x, y) = (0, 0)$, $(-80, 0)$, $(40, -69)$, and $(40, 69)$ ($z = 30$ mm for all) predicted with the linearized joint space FRFs from Eq. 28 (left) and measured at carriage C of the Monoprice Delta Pro 3D printer (right).

across their volume. Accounting for such detail is cumbersome because individual components would need to be disassembled and reassembled. We endeavored to be as accurate as possible, while ensuring that our methodology can be replicated without significant difficulty. However, we found that changes of a few millimeters in the end-effector center of mass location (especially in the z-direction) could significantly influence the magnitude and phase of the predicted FRFs. Secondly, the various joint connections between the end-effector, forearms, and carriages create friction that is difficult to capture via our least squares identification methodology.

The proposed model is intended for use in feedforward control of the delta 3D printer. Without this predictive model, an alternative approach for the control designer is to choose one baseline model with which to implement a model-based controller for the printer across the entire workspace. A reasonable choice for the baseline model is the measured FRF when the end-effector is positioned at $(x, y) = (0, 0)$ mm. To compare this alternative to using the predictive model, we study the percentage of reduction in model error attained by using the predictive model. Using μ_{err} defined in Eq. 71, the percentage error reduction can be defined as

$$\%\ \text{error reduction} = \frac{\mu_{err,B} - \mu_{err,P}}{\mu_{err,B}} \cdot 100 \tag{72}$$

where $\mu_{err,B}$ and $\mu_{err,P}$ are the mean absolute percentage errors of the baseline and predicted model, respectively. The expression for $\mu_{err,P}$ is identical to μ_{err} in Eq. 71, but for $\mu_{err,B}$, the baseline model is substituted for the prediction model, P_f. Table III reports the percentage error reduction when the predictive model is used to represent the measured FRFs at $(x, y) = (-80, 0)$, $(40, -69)$ and $(40, 69)$ mm instead of using the baseline model. From Figs. 11-13 and Table III, note that in most instances the predictive model predicts the magnitude and phase of the measured model more accurately than the baseline model. The baseline model has less magnitude or phase error compared to the predicted model at positions where the measured model and the baseline model have small differences (for the respective carriage). One expects there will be a few positions like this across the workspace. Importantly, at the position furthest along each carriage's line-of-action (diagonal entries in Table III), the predicted FRFs reduce the magnitude error by over 30% compared to the baseline and reduce the phase error by at least 14% and up to about 60%. These results suggest that naively choosing a baseline model to use in model-based feedforward control would result in worse accuracy performance when compared to using the LPV model proposed in this paper.

VI. CONCLUSION

The delta 3D printer offers the potential for higher throughput compared to traditional serial-axis 3D printers. However, it has not benefited from the model-based feedforward vibration compensation methods that have improved the accuracy and speed of serial 3D printers because of the difficulty modeling delta's nonlinear dynamics that vary as a function of position. In this paper, we propose an efficient framework that uses receptance coupling to identify LPV models for delta 3D printers using a few measurements from only one position. We generalize the model to account for different mass distributions and dynamic models of the end-effector, which can have a significant impact on the model, as demonstrated from measured data.

We presented the generalized model, described a procedure to identify its parameters, and demonstrated its efficacy using a commercial delta 3D printer, showing that the resulting model captures the position-dependent dynamic variations with reasonable accuracy. Additionally, at positions where the dynamics of the printer differ from the center (or baseline) model, we showed that the proposed model predicts the true dynamics with greater accuracy than the baseline model. In future work, we plan to implement a model-based controller on the delta 3D printer using the LPV model derived in this paper.

ACKNOWLEDGMENT

The authors would like to thank Abdul Hasib for helping design and manufacture the direct-drive extruder and Keval S. Ramani for useful feedback and discussions on modeling the end-effector.

REFERENCES

[1] R. Clavel, "Conception d'un robot parallèle rapide à 4 degrés de liberté," Ph.D. thesis, Dept. Microtechn., EPFL, Lausanne, Switzerland, 1991, doi: 10.5075/epfl-thesis-925.

[2] R. Clavel, "Device for the movement and positioning of an element in space," U.S. Patent 4 976 582, Dec. 11, 1990.

[3] J. Brinker and B. Corves, "A survey on parallel robots with delta-like architecture," in *Proc. 14th IFToMM World Congr.*, 2015, pp. 407–414, doi: 10.6567/IFToMM.14TH.WC.PS13.003.

[4] K. Miller, "Experimental verification of modeling of DELTA robot dynamics by direct application of Hamilton's principle," in *Proc. IEEE Int. Conf. Robot. Autom.*, May 1995, pp. 532–537, doi: 10.1109/ROBOT.1995.525338.

[5] M. A. Isa and I. Lazoglu, "Five-axis additive manufacturing of freeform models through buildup of transition layers," *J. Manuf. Syst.*, vol. 50, pp. 69–80, Jan. 2019, doi: 10.1016/j.jmsy.2018.12.002.

[6] R. J. A. Allen and R. S. Trask, "An experimental demonstration of effective curved layer fused filament fabrication utilising a parallel deposition robot," *Additive Manuf.*, vol. 8, pp. 78–87, Oct. 2015, doi: 10.1016/j.addma.2015.09.001.

[7] *Monoprice 3D Printers*. Accessed: Apr. 25, 2022. [Online]. Available: https://www.monoprice.com/

[8] *FLSUN*. Accessed: Apr. 25, 2022. [Online]. Available: https://flsun3d.com/

[9] *World Advanced Saving Project (WASP)*. Accessed: Apr. 25, 2022. [Online]. Available: https://www.3dwasp.com/en/

[10] *Tractus 3D*. Accessed: Apr. 25, 2022. [Online]. Available: https://amtech3d.com/tractus3d/

[11] K. S. Ramani, N. Edoimioya, and C. E. Okwudire, "A robust filtered basis functions approach for feedforward tracking control—With application to a vibration-prone 3-D printer," *IEEE/ASME Trans. Mechatronics*, vol. 25, no. 5, pp. 2556–2564, Oct. 2020, doi: 10.1109/TMECH.2020.2983680.

[12] M. Duan, D. Yoon, and C. E. Okwudire, "A limited-preview filtered B-spline approach to tracking control—With application to vibration-induced error compensation of a 3D printer," *Mechatronics*, vol. 56, pp. 287–296, Dec. 2018, doi: 10.1016/j.mechatronics.2017.09.002.

[13] H. Kim and C. E. Okwudire, "Simultaneous servo error pre-compensation and feedrate optimization with tolerance constraints using linear programming," *Int. J. Adv. Manuf. Technol.*, vol. 109, nos. 3–4, pp. 809–821, Jul. 2020, doi: 10.1007/s00170-020-05651-w.

[14] C. E. Okwudire, S. Huggi, S. Supe, C. Huang, and B. Zeng, "Low-level control of 3D printers from the cloud: A step toward 3D printer control as a service," *Inventions*, vol. 3, no. 3, p. 56, 2018, doi: 10.3390/inventions3030056.

[15] N. Edoimioya, K. S. Ramani, and C. E. Okwudire, "Software compensation of undesirable racking motion of H-frame 3D printers using filtered B-splines," *Additive Manuf.*, vol. 47, Nov. 2021, Art. no. 102290, doi: 10.1016/j.addma.2021.102290.

[16] A. Codourey, "Dynamic modeling of parallel robots for computed-torque control implementation," *Int. J. Robot. Res.*, vol. 17, no. 12, pp. 1325–1336, Dec. 1998, doi: 10.1177/027836499801701205.

[17] K. Miller, "Optimal design and modeling of spatial parallel manipulators," *Int. J. Robot. Res.*, vol. 23, no. 2, pp. 127–140, Feb. 2004, doi: 10.1177/0278364904041322.

[18] G. Lebret, K. Liu, and F. L. Lewis, "Dynamic analysis and control of a Stewart platform manipulator," *J. Robotic Syst.*, vol. 10, no. 5, pp. 629–655, 1993, doi: 10.1002/rob.4620100506.

[19] H. Pang and M. Shahinpoor, "Inverse dynamics of a parallel manipulator," *J. Robotic Syst.*, vol. 11, no. 8, pp. 693–702, 1994, doi: 10.1002/rob.4620110803.

[20] C.-D. Zhang and S.-M. Song, "An efficient method for inverse dynamics of manipulators based on the virtual work principle," *J. Robotic Syst.*, vol. 10, no. 5, pp. 605–627, Jul. 1993, doi: 10.1002/rob.4620100505.

[21] Q. Zhao, P. Wang, and J. Mei, "Controller parameter tuning of delta robot based on servo identification," *Chin. J. Mech. Eng.*, vol. 28, no. 2, pp. 267–275, Mar. 2015, doi: 10.3901/CJME.2014.1117.169.

[22] Y. Zhiyong and H. Tian, "A new method for tuning PID parameters of a 3 DoF reconfigurable parallel kinematic machine," in *Proc. IEEE Int. Conf. Robot. Autom. (ICRA)*, Apr. 2004, pp. 2249–2254, doi: 10.1109/ROBOT.2004.1307396.

[23] M. Ramírez-Neria, H. Sira-Ramírez, A. Luviano-Juárez, and A. Rodrguez-Ángeles, "Active disturbance rejection control applied to a delta parallel robot in trajectory tracking tasks," *Asian J. Control*, vol. 17, no. 2, pp. 636–647, Mar. 2015, doi: 10.1002/asjc.912.

[24] L. A. Castañeda, A. Luviano-Juárez, and I. Chairez, "Robust trajectory tracking of a delta robot through adaptive active disturbance rejection control," *IEEE Trans. Control Syst. Technol.*, vol. 23, no. 4, pp. 1387–1398, Jul. 2015, doi: 10.1109/TCST.2014.2367313.

[25] J. M. Escorcia-Hernandez, H. Aguilar-Sierra, O. Aguilar-Mejia, A. Chemori, and J. H. Arroyo-Nunez, "An intelligent compensation through B-spline neural network for a delta parallel robot," in *Proc. 6th Int. Conf. Control, Decis. Inf. Technol. (CoDIT)*, Apr. 2019, pp. 361–366, doi: 10.1109/CoDIT.2019.8820472.

[26] P. Chiacchio, F. Pierrot, L. Sciavicco, and B. Siciliano, "Robust design of independent joint controllers with experimentation on a high-speed parallel robot," *IEEE Trans. Ind. Electron.*, vol. 40, no. 4, pp. 393–403, Aug. 1993, doi: 10.1109/41.232228.

[27] L. Angel and J. Viola, "Fractional order PID for tracking control of a parallel robotic manipulator type delta," *ISA Trans.*, vol. 79, pp. 172–188, Aug. 2018, doi: 10.1016/j.isatra.2018.04.010.

[28] C. E. Boudjedir, D. Boukhetala, and M. Bouri, "Nonlinear PD plus sliding mode control with application to a parallel delta robot," *J. Electr. Eng.*, vol. 69, no. 5, pp. 329–336, Sep. 2018, doi: 10.2478/jee-2018-0048.

[29] Y. Su, D. Sun, L. Ren, and J. Mills, "Integration of saturated PI synchronous control and PD feedback for control of parallel manipulators," *IEEE Trans. Robot.*, vol. 22, no. 1, pp. 202–207, Feb. 2006, doi: 10.1109/TRO.2005.858852.

[30] R. Voorhoeve, R. de Rozario, W. Aangenent, and T. Oomen, "Identifying position-dependent mechanical systems: A modal approach applied to a flexible wafer stage," *IEEE Trans. Control Syst. Technol.*, vol. 29, no. 1, pp. 194–206, Jan. 2021, doi: 10.1109/TCST.2020.2974140.

[31] Y.-P. Liu and Y. Altintas, "Predicting the position-dependent dynamics of machine tools using progressive network," *Precis. Eng.*, vol. 73, pp. 409–422, Jan. 2022, doi: 10.1016/j.precisioneng.2021.10.010.

[32] T. L. Schmitz and K. S. Smith, "Receptance coupling," in *Mechanical Vibrations*. Boston, MA, USA: Springer, 2012, doi: 10.1007/978-3-030-52344-2_10.

[33] S. S. Park, Y. Altintas, and M. Movahhedy, "Receptance coupling for end mills," *Int. J. Mach. Tools Manuf.*, vol. 43, no. 9, pp. 889–896, 2003, doi: 10.1016/S0890-6955(03)00088-9.

[34] M. Law and S. Ihlenfeldt, "A frequency-based substructuring approach to efficiently model position-dependent dynamics in machine tools," *Proc. Inst. Mech. Eng., K, J. Multi-Body Dyn.*, vol. 229, no. 3, pp. 304–317, Sep. 2015, doi: 10.1177/1464419314562264.

[35] N. Edoimioya and C. E. Okwudire, "An efficient control-oriented modeling approach for vibration-prone delta 3D printers using receptance coupling," in *Proc. IEEE 17th Int. Conf. Autom. Sci. Eng. (CASE)*, Aug. 2021, pp. 165–170, doi: 10.1109/CASE49439.2021.9551537.

[36] Z. Ji, "Study of the effect of leg inertia in Stewart platforms," in *Proc. Int. Conf. Robot. Autom.*, 1993, pp. 121–126, doi: 10.1109/ROBOT.1993.291971.

[37] A. Moetazedian, A. S. Budisuharto, V. V. Silberschmidt, and A. Gleadall, "CONVEX (CONtinuously Varied EXtrusion): A new scale of design for additive manufacturing," *Additive Manuf.*, vol. 37, Jan. 2021, Art. no. 101576, doi: 10.1016/j.addma.2020.101576.

Nosakhare Edoimioya received the B.S. degree in mechanical engineering from Stanford University in 2017 and the M.S. degree in mechanical engineering from the University of Michigan in 2019, where he is currently pursuing the Ph.D. degree in mechanical engineering. His research interests include mechatronics systems design and control for improved performance of additive manufacturing machines. He was awarded the National Science Foundation GRFP Award in 2018 and the Michigan Space Grant Consortium Graduate Student Fellowship in 2019.

Chinedum E. Okwudire (Member, IEEE) received the Ph.D. degree in mechanical engineering from The University of British Columbia in 2009. He joined the Mechanical Engineering Faculty, University of Michigan, in 2011. Prior to joining Michigan, he was the Mechatronic Systems Optimization Team Leader with DMG Mori USA, Davis, CA, USA. His research is focused on exploiting knowledge at the intersection of machine design, control and, more-recently, computer science, to boost the performance of manufacturing automation systems at low cost. He has received a number of awards including the CAREER Award from the National Science Foundation, the Young Investigator Award from the International Symposium on Flexible Automation, the Outstanding Young Manufacturing Engineer Award from the Society of Manufacturing Engineers, the Ralph Teetor Educational Award from SAE International, and the Russell Severance Springer Visiting Professorship from UC Berkeley. He has coauthored a number of best paper award winning papers in the areas of control and mechatronics.